coatings

MDPI

Article

Finite-Difference Time-Domain Simulation of Double-Ridge Superimposed Structures for Optimizing Light-Trapping Characteristics in Ternary Organic Solar Cells

Xiaoxiang Sun, Jinglin Song, Weijun Tan, Jing Chen, Mingxin Chen, Fen Li, Chang Li * and Zhuoliang Yu *

Key Laboratory of Hunan Province on Information Photonics and Freespace Optical Communications, College of Physics and Electronics, Hunan Institute of Science and Technology, Yueyang 414006, China
* Correspondence: lichang@hinst.edu.com (C.L.); 12021016@hnist.edu.cn (Z.Y.)

Abstract: The double-ridge superimposed structures (DRSSs), formed by the superposition of a nano-ridged textured ZnO layer and a ternary organic active layer (PTB7:$PC_{70}BM$:$PC_{60}BM$) with self-assembled nano-ridged (SANR) structures, have been preliminarily examined experimentally for its positive effects in light-trapping for organic solar cells (OSCs). To obtain DRSSs with higher-performance light-trapping effects and enhance the light absorption of OSCs, the present work carried out prior theoretical simulations of the light-trapping characteristics of the DRSS using the finite-difference time-domain (FDTD) algorithm. The results show that the DRSS exhibits a significant light-trapping effect, with an active layer absorption peak around 530 nm due to the light-trapping effect. This helps the active layer capture more high-energy photons, significantly enhancing the photon utilization of the DRSS. Interestingly, the intensity of the light-trapping absorption peak is solely dependent on the height or width of the active layer ridges in the DRSS, while the position of the peak is jointly determined by both the ZnO and active layer ridges. By controlling the aspect ratio (W/H) of the dual ridges, the light-trapping absorption peak position can be fine-tuned, enabling precise light-trapping management for specific wavelength bands. It is certain that the outcomes of this work will provide theoretical foundations and practical guidance for the fabrication of light-trapping OSCs.

Keywords: ternary organic film; double-ridge superimposed structures; light-trapping characteristics; FDTD method

Citation: Sun, X.; Song, J.; Tan, W.; Chen, J.; Chen, M.; Li, F.; Li, C.; Yu, Z. Finite-Difference Time-Domain Simulation of Double-Ridge Superimposed Structures for Optimizing Light-Trapping Characteristics in Ternary Organic Solar Cells. *Coatings* **2024**, *14*, 1583. https://doi.org/10.3390/coatings14121583

Academic Editor: Michel Voué

Received: 21 November 2024
Revised: 13 December 2024
Accepted: 17 December 2024
Published: 18 December 2024

1. Introduction

Substantial progress has been achieved in the domain of organic solar cells (OSCs), driven by recent breakthroughs in active layer materials and device structure optimization. These advancements have catalyzed a remarkable increase in their power conversion efficiency (PCE), pushing it to the brink of 20% [1–3]. Nonetheless, compared to other emerging solar cell technologies, OSCs still do not offer a significant efficiency advantage [4,5]. Consequently, improving the PCE remains a major challenge for OSCs. The bottlenecks faced by OSCs primarily stem from two aspects. On one hand, increasing the thickness of the active layer can enhance photon absorption, but this also has negative effects, such as hindering the separation of excitons and increasing the probability of electron–hole recombination [6–8]. Currently, most reported OSCs have an active layer thickness of about 100 nm [9–11], which is much thinner than the light-absorbing layers in other types of thin-film solar cells. Therefore, achieving efficient photon absorption within the constraints of a limited active layer thickness is crucial for further improving the PCE. On the other hand, synthesizing new organic materials with high mobility could significantly increase the thickness of the active layer [12–14]. It has been shown that devices using new organic materials with high mobility can exhibit PCEs greater than 14% even when the active layer thickness exceeds 200 nm [15] or even reaches 400 nm [16]. However, the development

and use of these advanced organic materials will substantially raise the production costs of OSCs.

Light-trapping OSCs provide a solution to the aforementioned bottleneck issues by significantly enhancing the photon utilization of the devices through an efficient "light management" strategy while maintaining the original thickness of the active layer [17–20]. Light management in OSCs is mainly achieved by controlling the distribution of light paths, optical paths, and light field intensity. Depending on the location of the introduction of the trapped light structure, the light management methods in OSCs can be categorized into the following three types, i.e., optical isolation layer [21,22], surface patterning of the active layer [23,24], and trapped photovoltaic electrodes [25,26]. The above methods can indeed effectively reduce the transmission and reflection of photons in a specific wavelength range and thus enhance light absorption, but there are also some unavoidable problems [27–30]. For example, the screening and preparation of optical isolation materials is extremely stringent; the surface patterning technology is complicated, which easily leads to the formation of Schottky contact between the active layer and the electrode, impeding the collection of carriers by the electrode and easily destroying the structure of the active layer; and the trapped photoelectrode involves a complex pre-treatment or processing process, which will impede the close contact between the electrode and the active layer.

Instead, we have reported a more convenient and effective strategy of the ternary organic active layer (PTB7:$PC_{70}BM$:$PC_{60}BM$) with the self-assembled nano-ridged (SANR) structures [31,32]. Our studies have shown that when the content of $PC_{60}BM$ in fullerenes is exactly equal to 50%, the distinct SANR structures will appear in the ternary active layer, and both experimental and theoretical studies have demonstrated that the SANR structures have an obvious light-trapping effect, which significantly enhances the absorption of photons in a specific wavelength range, and thus enhances the short-circuit current density (J_{sc}) of the devices. In addition, we have also experimentally verified the positive effect of the double-ridge superimposed structures (DRSSs) on the light-trapping characteristics. The DRSS is formed by the superposition of the nano-ridged textured ZnO and the PTB7:$PC_{70}BM$:$PC_{60}BM$ blend film with the SANR structures, which can further enhance the absorption of photons in the wavelength range of 500–700 nm on the basis of the SANR structures [31]. Compared to other light management strategies, the DRSS stands out due to the simplicity, repeatability, and non-destructiveness of its preparation process. The SANR structures form spontaneously during the spin-coating process, eliminating the need for any post-processing steps. Additionally, the textured ZnO can be easily obtained through a straightforward combination of spin-coating and gradient annealing. Consequently, the DRSS offers maximum protection to the active layer, preventing any potential damage, while ensuring smooth and efficient subsequent device fabrication processes. However, the light-trapping effect and characteristics of the DRSS are still to be further investigated, thus realizing more efficient photon absorption and helping OSCs to break through the bottleneck and obtain higher PCE.

In order to experimentally prepare the DRSS with a high-performance light-trapping effect, the present work carried out prior theoretical simulations of the light-trapping characteristics of the DRSS using the finite-difference time-domain (FDTD) algorithm. The results show that the DRSS exhibits a more significant light-trapping effect compared to the single-layer ZnO ridges and the single-layer PTB7:$PC_{70}BM$:$PC_{60}BM$ ridges. The active layer absorption peak due to the light-trapping effect can help the active layer capture more high-energy photons, thus significantly enhancing the photon utilization of the DRSS. In addition, the intensity of the light-trapping absorption peak is solely dependent on the height or width of the active layer ridges in the DRSS. However, the position of the light-trapping absorption peak is jointly determined by both the ZnO and active layer ridges. By simultaneously controlling the aspect ratio (W/H) of the ZnO and active layer dual ridges, fine-tuning of the light-trapping absorption peak position can be achieved, thereby enabling precise light-trapping management for specific wavelength bands.

2. Simulation Model and Methods

2.1. Numerical Conditions and Parameters

The simulation employed the FDTD algorithm [32,33], a rigorous method for solving Maxwell's equations, which yields the electromagnetic field distribution over time and space. All simulation regions were configured with periodic boundary conditions along the X- and Y-axes to maintain continuity, while perfectly matched layers (PMLs) were used along the *Z*-axis to absorb outgoing waves without generating reflections back into the simulation area [34]. An incident plane wave with a wavelength range from 200 to 900 nm served as the electromagnetic source, propagating directly along the *Z*-axis from the ZnO layer. Reflectance (R) and transmittance (T) were measured using infinite sensors that captured all reflected and transmitted energies, respectively, with absorptance calculated as 1-R-T. These sensors were strategically positioned far enough from the device to avoid any near-field effects [35]. Accuracy in the simulation results was critically dependent on precise dispersion curves of the complex refractive indices of the materials used. The real (n) and imaginary (k) parts of the complex refractive index for the ZnO and PTB7:PC_{70}BM:PC_{60}BM films were derived from the detailed research of Dias [36] and Shim [37], ensuring high fidelity and accuracy in simulating the optical properties of the materials.

2.2. Numerical Model

The construction of a high-fidelity equivalent numerical model is crucial for ensuring the reliability of simulation results. In this work, the formulation of the equivalent numerical model is based on atomic force microscope (AFM) scans of the textured ZnO and SANR structures, as detailed in Figure S1. These scans reveal that both the textured ZnO and the active layer exhibit a randomly oriented ridge-like morphology. For additional insights into the textured ZnO and SANR structures, please consult our previous publication [31]. Given the morphological traits of the textured ZnO and SANR structures, we devised a primitive equivalent numerical model of the DRSS, as illustrated in Figure 1a. The textured ZnO comprises a rectangular base (height 30 nm) and multiple isosceles triangular prisms (height 50 nm) on top, with each isosceles triangular prism measuring 425 nm in the *X*-direction (width) and 1000 nm in the *Y*-direction (length). It is worth noting that there is no space between adjacent isosceles triangular prisms. Following this, a conformed textured active layer with a thickness of 80 nm was applied onto the textured ZnO. The side view of the simulation model's unit cell is displayed in Figure 1b. Additionally, for comparative analysis, we built three other equivalent numerical models, as depicted in Figure 2a. Specifically, Model A exhibits flat ZnO with a flat active layer, Model B features textured ZnO with a flat active layer, and Model C showcases flat ZnO with a textured active layer. It is imperative to highlight that the equivalent volume (mass) of the active layer is consistent across all four models to eliminate any effects caused by variations in the thickness of the light-absorbing layer.

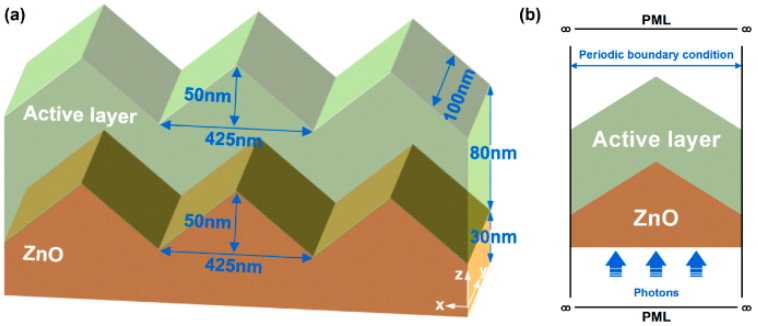

Figure 1. (**a**) Schematic diagram of the numerical model of the DRSS. (**b**) The side view of the simulation model's unit cell.

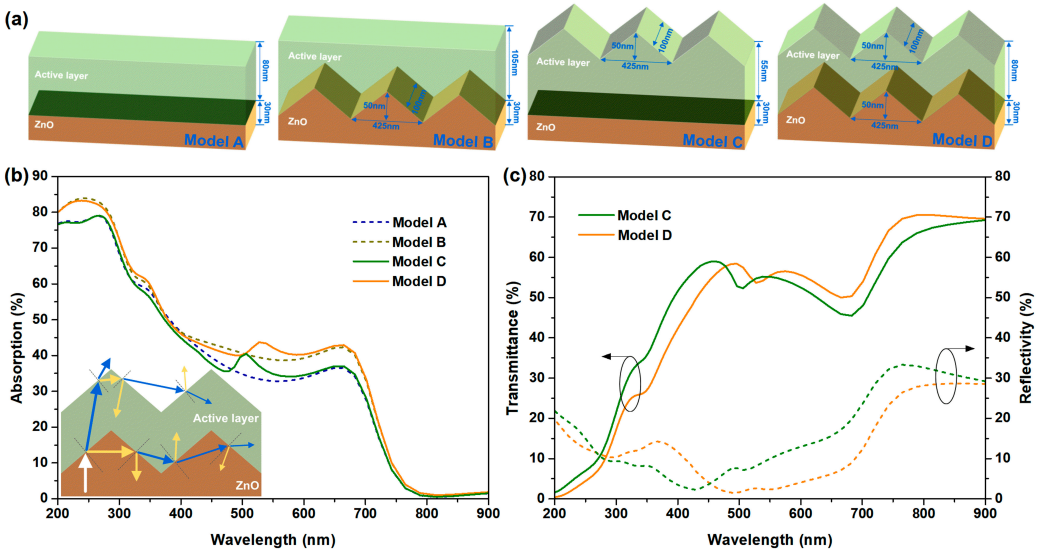

Figure 2. (**a**) Schematic diagram of the different models. (**b**) Absorption spectra of the different models; the inset shows the light-trapping mechanism of the DRSS. (**c**) Corresponding transmission and reflection spectra.

3. Results and Discussion

Our previous work has preliminarily demonstrated the light-trapping effect of the DRSS, but there is still a need for a more comprehensive understanding of its light-trapping characteristics. In this work, we used the FDTD algorithm to carry out prior simulation research on the DRSS. The absorption spectra of the four models are given in Figure 2b, and a comparative analysis reveals that the introduction of textured structures can effectively enhance photon absorption in a specific wavelength range. In Model B, the introduction of ZnO ridges leads to a significant increase in photon absorption in the wavelength range of 420–700 nm, which is attributed to the fact that the introduction of the ridge structures significantly reduces the reflection of incident photons by the ZnO layer, which leads to more photons entering the active layer to be absorbed (as shown in Figure S2). In Model C, the introduction of ridges in the active layer results in a pronounced absorption peak at 500 nm. Typically, the absorption peaks of the PTB7:PC_{70}BM:PC_{60}BM blend film occur around 620–680 nm and mainly stem from photon absorption by PTB7 [38,39]. Therefore, it is reasonable to infer that the absorption peak at 500 nm is due to the light-trapping effect induced by the ridges (a more detailed discussion follows). In Model D, the introduction of the DRSS causes a redshift (530 nm) in the absorption peak. More importantly, compared to Model C, photon absorption in the wavelength range of 400–700 nm is significantly improved. Clearly, the addition of ZnO ridges further enhances the light-trapping performance of the active layer. From the transmission and reflection spectra, as shown in Figure 2c, it is evident that the DRSS has a significant impact on both transmission and reflection spectra. Firstly, the appearance and redshift of the light-trapping absorption peak are mainly attributed to the significant reduction in transmission at 500 nm and 530 nm. Secondly, the enhanced photon absorption in the wavelength range of 450–700 nm is due to the significant reduction in reflection. Indeed, our previous experimental studies have revealed that the presence of the DRRS significantly reduces the reflectivity of the devices for photons in the wavelength range of 500–700 nm [31], and this result has now been verified theoretically. It is evident that the incorporation of ridge structures significantly increases the frequency of photon reflections and refractions at the interface. As a result, the photons are trapped within the active layer through these reflections and refractions, as illustrated in the inset of Figure 2a. This prolongs the optical path length of the photons within the active layer, thereby substantially enhancing their absorption probability [32].

Figure 3 presents the cross-section images of the electric field intensity $|E|^2$ distribution at an incident wavelength of 520 nm for the different models. The results illustrate that

the presence of the ridge structures can influence the optical field distribution of incident light within the active layer. The presence of ridge-like structures traps more high-energy photons in the active layer, thus increasing the chance of photon absorption by the active layer [40]. In Model D, a large number of high-energy photons are trapped at the junctions of neighboring ridge-like structures, especially at the top of the active layer, which explains why Model D shows an obvious absorption peak at 520 nm. In fact, this phenomenon of high-energy photons being trapped at the top of the active layer is also present in Model C, as shown in Figure S3, which also leads to a significant absorption peak at 500 nm (shown in Figure 2b).

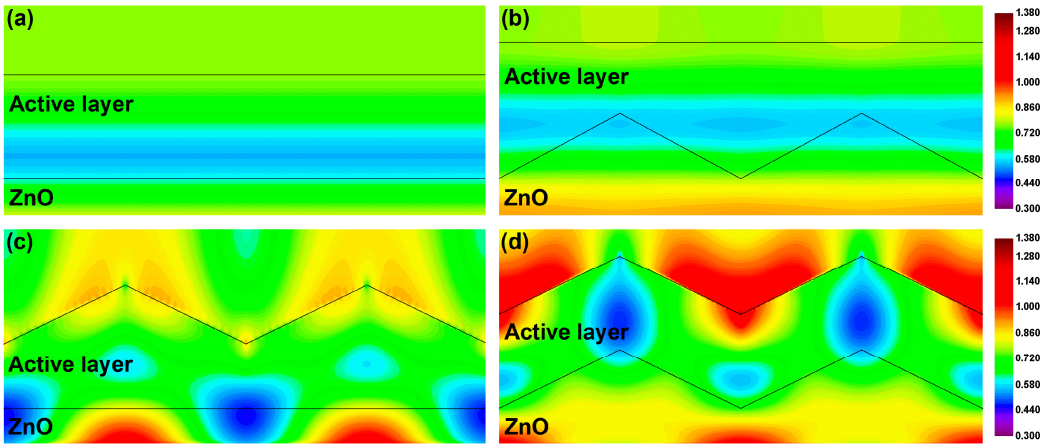

Figure 3. The normalized cross-section near-field profiles of TM-polarized light for normal-incidence monochromatic illumination at the wavelength of 520 nm in the different models. (**a**) Model A, (**b**) Model B, (**c**) Model C, and (**d**) Model D.

Having clarified the light-trapping effect of the DRSS, it is necessary to further explore its light-trapping characteristics. First, on the basis of the original equivalent numerical model of the DRSS, the dimensions of the ZnO ridges were kept constant (50 nm in height and 425 nm in width), and the influence of the change in the width of the active layer ridges on the light-trapping effect was investigated, and the equivalent numerical model is shown in the inset in Figure 4a. From the absorption spectra, it can be seen that the intensity of the light-trapping absorption peaks shows a tendency to strengthen and then weaken when the width of the ridge structure decreases from 425 nm to 75 nm, and the intensity reaches a maximum at a width of 325 nm. It is noteworthy that the light-trapping absorption peak disappears when the width is reduced to 75 nm, which means that the light-trapping effect no longer exists. From Figure 4b, it can be found that the intensity change of the light-trapping absorption peaks mainly originates from the effect of the width change of the ridge structures on the transmittance. The transmittance changes significantly only near 530 nm, while the corresponding transmittance at other wavelengths is almost unaffected by the width variation. In addition, the effect of the width variation on the reflectance is essentially negligible.

Based on the above results, we continue to explore the influence of the change in the height of the active layer ridges (325 nm in width) on the effect of light trapping, and the equivalent numerical model is shown in the inset in Figure 5a. The results of the absorption spectra show that the intensity of the light-trapping absorption peaks gradually decreases as the height of the ridges decreases, and no obvious absorption peaks can be observed when the height decreases to 10 nm, which implies the disappearance of the light-trapping effect. Clearly, the elevation in height inherently amplifies the surface roughness of the active layer, with a rougher surface exhibiting enhanced light-trapping capabilities [41]. At the same time, the absorption in the wavelength range of 310–360 nm is enhanced to some extent with the increase in height. From the results of transmission and reflection spectra, it can be analyzed that the enhancement of photon absorption in the wavelength range of

310–360 nm is due to the decrease in reflectivity, while the enhancement of the absorption peak (530 nm) is due to the decrease in transmittance.

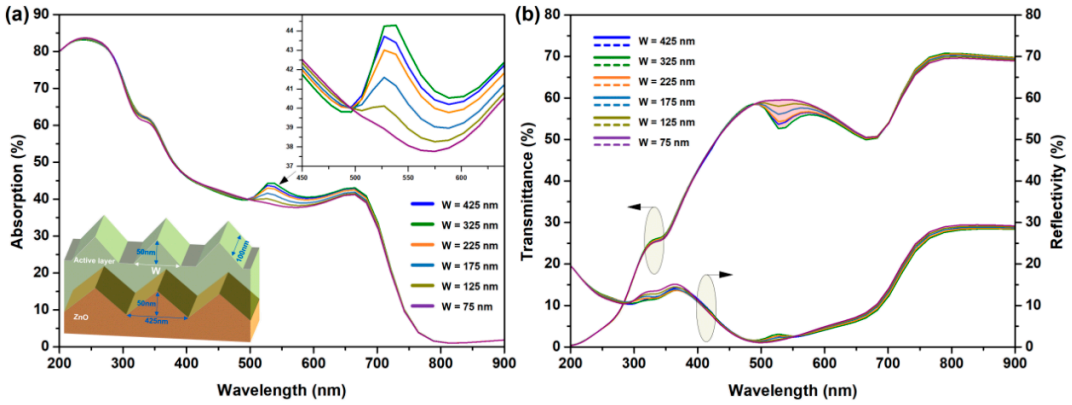

Figure 4. Optical properties of the DRSS with different active layer texture morphologies; the size of the ZnO ridge structures is constant and the height of the active layer ridge structures is fixed at 50 nm. (**a**) Absorption spectra. (**b**) Transmission and reflection spectra.

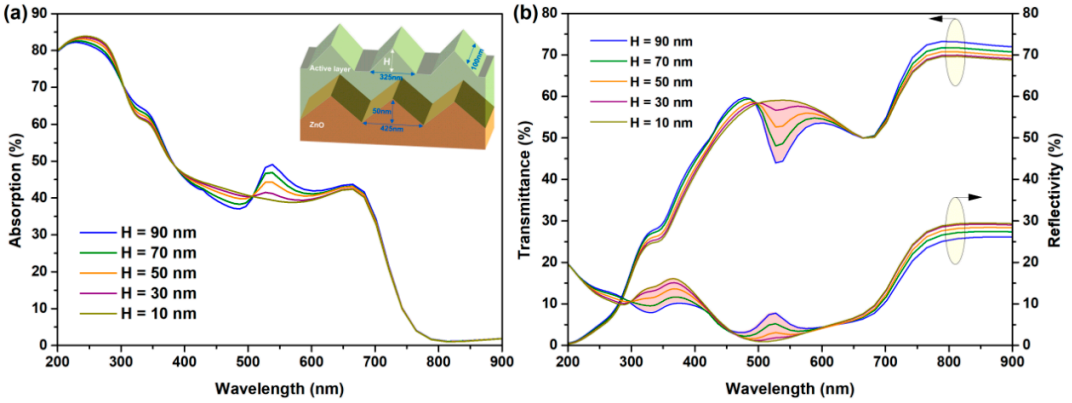

Figure 5. Optical properties of the DRSS with different active layer texture morphologies; the size of the ZnO texture structure is constant and the width of the active layer texture structure is fixed at 325 nm. (**a**) Absorption spectra. (**b**) Transmission and reflection spectra.

Combining the results of Figures 4 and 5, it can be inferred that the variation in the width of the active layer ridges mainly affects the transmission of photons, while the variation in the height has a large effect on both transmission and reflection. In addition, the appearance of the light-trapping effect is related to the width and height of the active layer ridges, and both the width and height are too small to lead to the disappearance of the light-trapping effect. For example, when the height is 90 nm, the light-trapping effect is very significant with sharp absorption peaks (as shown in Figure 5a), but even so, the light-trapping effect disappears when the width is reduced to 75 nm, as shown in Figure S4. In fact, a reduction in the height of the ridges leads to a reduction in the surface roughness of the active layer, and the surface tends to be flat, at which point the equivalent numerical model is similar to that of Model B. Therefore, as illustrated in Figure 6a, the photon distribution in the active layer is similar to that in Model B (as shown in Figure 3b), and no high-energy photons are observed in the active layer. Similarly, reducing the width of the ridges also flattens the surface, as depicted in Figure 6c, resulting in the absence of high-energy photons in the active layer. Furthermore, the ridges trap a large number of low-energy photons, which inevitably leads to a reduction in absorption. Clearly, as shown in Figure 6b, only an active layer with a large roughness can exhibit a significant light-trapping effect, trapping a large number of high-energy photons and thus enhancing photon absorption.

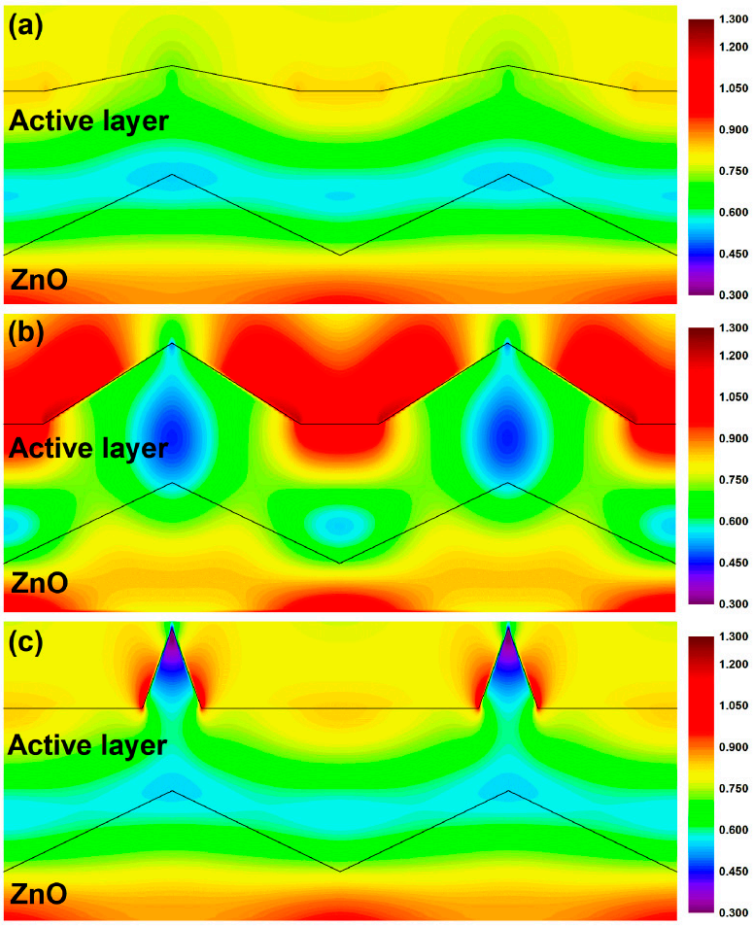

Figure 6. The normalized near-field profiles of TM-polarized light for normal-incidence monochromatic illumination at a wavelength of 520 nm, observed in the DRSS with different active layer texture morphologies; the size of the ZnO texture structure is constant. (**a**) H = 10 nm and W = 325 nm; (**b**) H = 50 nm and W = 325 nm; (**c**) H = 50 nm and W = 75 nm.

Interestingly, when the dimensions of the active layer ridges remain constant, changes in the dimensions (height and width) of the ZnO ridges have almost no impact on the absorption spectrum of the DRSS, as shown in Figure S5. However, this does not imply that the dimensions of the ZnO ridges can be neglected, as subsequent research will reveal the important role played by the ZnO ridges in the DRSS. It is essential to investigate the effect of simultaneous changes in the dimensions of both the ZnO and active layer dual ridges on the light-trapping characteristics of the DRSS. Initially, the effect of the synchronized change in height was investigated by fixing the width of the ZnO and active layer dual ridges at 425 nm, and the detailed numerical model is illustrated in the inset in Figure 7a. Obviously, as depicted in Figure 7a, the simultaneous increase in the height of the ridges enhances the photon absorption in both the short-wavelength band (220–350 nm) and the long-wavelength band (500–700 nm), thereby realizing a broad-spectrum photon response. It can also be observed that the light-trapping absorption peaks are redshifted, and the higher the ridges, the easier it is to capture low-energy photons in the long-wavelength band. From the transmission and reflection spectra, as depicted in Figure 7b, it can be seen that the enhancement in the short- and long-wavelength bands is attributed to the reduction in transmittance and reflectance, respectively. Furthermore, it can be determined that the enhancement of photon absorption is a result of the synergistic effect of the ZnO and active layer dual ridges. As revealed in Figure S6, in Model B, when the height of the ZnO ridges is increased, the photon absorption in both the short- and long-wavelength bands is significantly enhanced, but the light-trapping absorption peak is never observed,

whereas when the active layer ridges are introduced (in Model D), the light-trapping absorption peak at ~530 nm is very significant, which further proves that the appearance of the light-trapping absorption peaks is a product of the light-trapping effect.

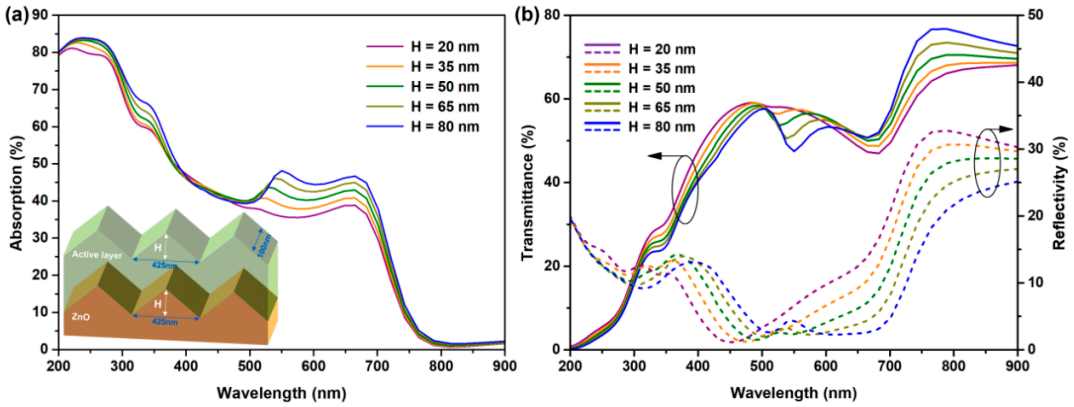

Figure 7. Optical properties of the DRSS with different ZnO and active layer texture morphologies; the width of the ZnO and active layer texture structures is fixed at 425 nm and the heights of both remain synchronized. (**a**) Absorption spectra. (**b**) Transmission and reflection spectra.

Next, the effect of simultaneous changes in the width of the ZnO and active layer dual ridges on the light-trapping characteristics of the DRSS was explored, and the specific numerical model is shown in the inset in Figure 8, with the height of the ridges fixed at 50 nm, so as to reveal the variation in the width of the ridges with respect to the absorption spectra. As revealed in Figure 8, there is a strong correlation between the position of the light-trapping absorption peak and the width of the ridges, where an increase in width will lead to a redshift of the light-trapping absorption peak, and a similar phenomenon is observed in Figure 7a, where an increase in height will lead to a redshift of the light-trapping absorption peak, but it is clear that the redshift is much more pronounced due to the change in width. Briefly, the results in Figures 7a and 8 illustrate that there is a strong correlation between the position of the light-trapping absorption peaks and the dimensions (height and width) of the dual ridges. Based on these results, it can be inferred that a finer regulation of the light-trapping absorption peaks can be achieved by simultaneous and synchronous regulation of the height and width of the dual ridges.

To verify the above inference, an in-depth study as shown in Figure 9 was executed to reveal the modulation behavior of the aspect ratio (W/H) on the light-trapping absorption peaks by simultaneously and synchronously varying the height and width of the ZnO and active layer dual ridges; the specific numerical model is shown in the inset in Figure 9a, and the detailed parameters of the W/H are displayed in Table 1. The results show that the light-trapping absorption peak undergoes a significant and well-documented redshift as the aspect ratio increases, as shown in Figure 9a. Indeed, the light-trapping mechanism of the DRSS is similar to that of an optical resonator when the height and width are varied simultaneously [42]. Obviously, fine-tuning of the light-trapping absorption peak positions can be achieved by fine-tuning the W/H of the ridges, which enables the light-trapping management of photons in a specific wavelength band. In addition, it can be seen from the transmission and reflection spectra, as shown in Figure 9b, that the appearance and redshift of the light-trapping absorption peaks mainly depend on the significant reduction and redshift of the transmission spectrum.

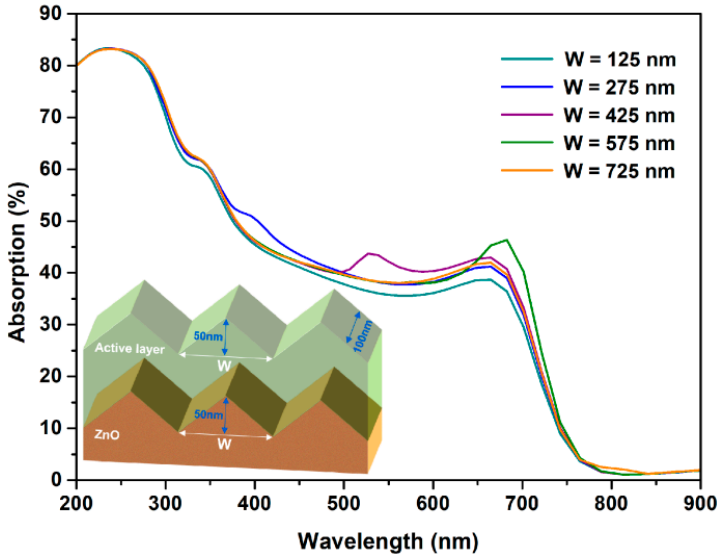

Figure 8. Absorption spectra of the DRSS with different ZnO and active layer texture morphologies; the height of the ZnO and active layer texture structures is fixed at 50 nm and the widths of both remain synchronized.

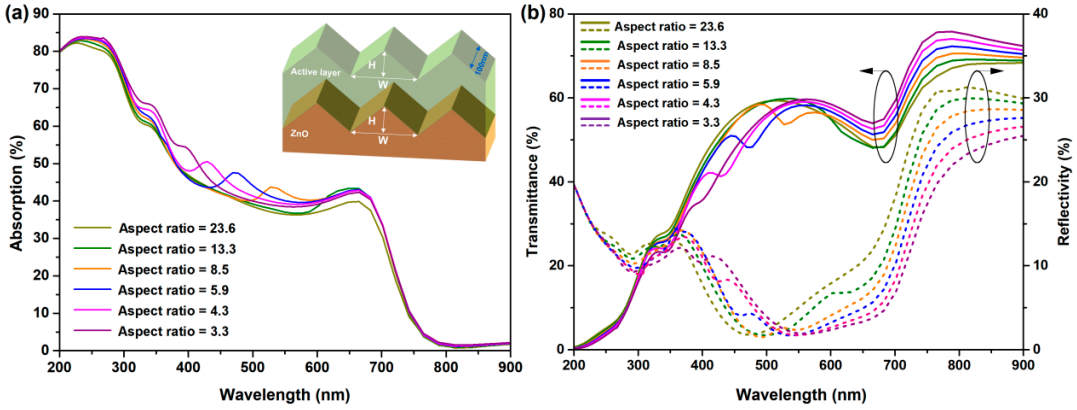

Figure 9. Optical properties of the DRSS with different ZnO and active layer texture morphologies; the height and width of the ZnO and active layer texture structures are kept synchronized, and the detailed aspect ratio settings are shown in Table 1. (**a**) Absorption spectra. (**b**) Transmission and reflection spectra.

Table 1. Detailed parameters for the DRSS with varying aspect ratios as depicted in Figure 9.

Height (nm)	Width (nm)	Aspect Ratio (W/H)
30	708	23.6
40	531	13.3
50	425	8.5
60	354	5.9
70	304	4.3
80	266	3.3

4. Conclusions

In conclusion, in order to experimentally prepare the DRSS (consisting of ZnO and PTB7:$PC_{70}BM$:$PC_{60}BM$ nano-ridged structures) with a high-performance light-trapping effect to enhance the light absorption of the OSCs, the present work carried out prior theoretical simulations of the light-trapping characteristics of the DRSS using the FDTD algorithm. The results show that the DRSS exhibits a more significant light-trapping effect

compared to the single-layer ZnO ridges and the single-layer PTB7:$PC_{70}BM$:$PC_{60}BM$ ridges. The active layer absorption peak (~530 nm) due to the light-trapping effect was successfully observed, and the light-trapping absorption peak can help the active layer capture more high-energy photons, thus significantly enhancing the photon utilization of the DRSS. In addition, the intensity of the light-trapping absorption peak is solely dependent on the height or width of the active layer ridges in the DRSS. When the dimensions of the active layer ridges remain constant, changes in the dimensions of the ZnO ridges do not affect the light-trapping performance of the DRSS. However, the position of the light-trapping absorption peak is jointly determined by both the ZnO ridges and the active layer ridges. When the heights or widths of the dual ridges are increased synchronously, noticeable redshifts in the light-trapping absorption peak will occur. By simultaneously controlling the aspect ratio (W/H) of the dual ridges, fine-tuning of the light-trapping absorption peak position can be achieved, thereby enabling precise light-trapping management for specific wavelength bands. Although precise control over the dimensions of the DRSS is currently a significant challenge, it is foreseeable that if different sizes of the DRSS can be successfully integrated within a single device, the device will be capable of enhancing wide-spectrum photon absorption. In short, the outcomes of this work will provide theoretical foundations and practical guidance for the fabrication of light-trapping OSCs.

Supplementary Materials: The following supporting information can be downloaded at: https://www.mdpi.com/article/10.3390/coatings14121583/s1, Figure S1. Top-view and side-view AFM images: (a) textured ZnO and (b) active layer with SANR structures. Figure S2. Transmission and reflection spectra of Model A and Model B. Figure S3. The normalized cross-section near-field profiles of TM-polarized light for normal-incidence monochromatic illumination at the wavelength of 500 nm in Model C. Figure S4. Absorption spectra of the DRSS with different active layer texture morphologies; the size of the ZnO texture structure is constant and the height of the active layer texture structure is fixed at 90 nm. Figure S5. Absorption spectra of the DRSS with different ZnO texture morphologies. The width is fixed at 425 nm when the height of the ZnO texture structure is varied, and the height is fixed at 50 nm when the width of the ZnO texture structure is varied. The active layer texture structures are fixed in size. Figure S6. Optical properties of Model B with different ZnO texture morphologies; the width of the ZnO texture structure is fixed at 425 nm. (a) Transmission and reflection spectra. (b) Absorption spectra.

Author Contributions: Conceptualization, C.L.; Investigation, W.T. and J.C.; Data curation, J.S. and M.C.; Writing—original draft, X.S.; Writing—review & editing, Z.Y.; Supervision, F.L. All authors have read and agreed to the published version of the manuscript.

Funding: This research was funded by the Education Department of Hunan Province (Grant No. 22B0687), the Hunan Provincial Natural Science Foundation of China (Grant No. 2023JJ30282), the National Natural Science Foundation of China (Grant No. 12274121), and the Training Program of Innovation and Entrepreneurship for Undergraduates of Hunan Province (Grant No. 3195). We acknowledge the financial support of the Science and Technology Program of Hunan Province (Grant No. 2019TP1014).

Institutional Review Board Statement: Not applicable.

Informed Consent Statement: Not applicable.

Data Availability Statement: Data are contained within the article and supplementary materials.

Conflicts of Interest: The authors declare no conflict of interest.

References

1. Chen, C.; Wang, L.; Xia, W.; Qiu, K.; Guo, C.; Gan, Z.; Zhou, J.; Sun, Y.; Liu, D.; Li, W.; et al. Molecular interaction induced dual fibrils towards organic solar cells with certified efficiency over 20%. *Nat. Commun.* **2024**, *15*, 6865. [CrossRef] [PubMed]
2. Fu, J.; Yang, Q.; Huang, P.; Chung, S.; Cho, K.; Kan, Z.; Liu, H.; Lu, X.; Lang, Y.; Lai, H.; et al. Rational molecular and device design enables organic solar cells approaching 20% efficiency. *Nat. Commun.* **2024**, *15*, 1830. [CrossRef] [PubMed]
3. Fu, J.; Fong, P.W.; Liu, H.; Huang, C.S.; Lu, X.; Lu, S.; Abdelsamie, M.; Kodalle, T.; Sutter-Fella, C.M.; Yang, Y.; et al. 19.31% binary organic solar cell and low non-radiative recombination enabled by non-monotonic intermediate state transition. *Nat. Commun.* **2023**, *14*, 1760. [CrossRef] [PubMed]

4. Lan, Z.R.; Wang, Y.D.; Shao, J.Y.; Ma, D.X.; Liu, Z.; Li, D.; Hou, Y.; Yao, J.; Zhong, Y.W. Surface passivation with diaminopropane dihydroiodide for p-i-n perovskite solar cells with over 25% efficiency. *Adv. Funct. Mater.* **2024**, *34*, 2312426. [CrossRef]
5. Panchanan, S.; Dastgeer, G.; Dutta, S.; Hu, M.; Lee, S.U.; Im, J.; Seok, S.I. Cerium-based halide perovskite derivatives: A promising alternative for lead-free narrowband UV photodetection. *Matter* **2024**, *7*, 3949–3969. [CrossRef]
6. Sun, X.; Li, C.; Ni, J.; Huang, L.; Xu, R.; Li, Z.; Cai, H.; Li, J.; Zhang, Y.; Zhang, J. A facile two-step interface engineering strategy to boost the efficiency of inverted ternary-blend polymer solar cells over 10%. *ACS Sustain. Chem. Eng.* **2017**, *5*, 8997–9005. [CrossRef]
7. Günther, M.; Kazerouni, N.; Blätte, D.; Perea, J.D.; Thompson, B.C.; Ameri, T. Models and mechanisms of ternary organic solar cells. *Nat. Rev. Mater.* **2023**, *8*, 456–471. [CrossRef]
8. Zhang, M.; Chang, B.; Zhang, R.; Li, S.; Liu, X.; Zeng, L.; Chen, Q.; Wang, L.; Yang, L.; Wang, H.; et al. Tethered small-molecule acceptor refines hierarchical morphology in ternary polymer solar cells: Enhanced stability and 19% efficiency. *Adv. Mater.* **2024**, *36*, 2308606. [CrossRef] [PubMed]
9. Lee, S.; Jeong, D.; Kim, C.; Lee, C.; Kang, H.; Woo, H.Y.; Kim, B.J. Eco-friendly polymer solar cells: Advances in green-solvent processing and material design. *ACS Nano* **2020**, *14*, 14493–14527. [CrossRef] [PubMed]
10. Sorrentino, R.; Kozma, E.; Luzzati, S.; Po, R. Interlayers for non-fullerene based polymer solar cells: Distinctive features and challenges. *Energy Environ. Sci.* **2021**, *14*, 180–223. [CrossRef]
11. Yao, H.; Hou, J. Recent advances in single-junction organic solar cells. *Angew. Chem. Int. Ed.* **2022**, *61*, e202209021. [CrossRef] [PubMed]
12. Wang, L.J.; Nan, G.J.; Yang, X.D.; Peng, Q.; Li, Q.K.; Shuai, Z.G. Computational methods for design of organic materials with high charge mobility. *Chem. Soc. Rev.* **2010**, *39*, 423–434. [CrossRef] [PubMed]
13. Wang, Y.F.; Liang, Z.Z.; Li, X.M.; Qin, J.C.; Ren, M.L.; Yang, C.Y.; Bao, X.C.; Xia, Y.J.; Li, J.F. Self-doping n-type polymer as a cathode interface layer enables efficient organic solar cells by increasing built-in electric field and boosting interface contact. *J. Mater. Chem. C* **2019**, *7*, 11152–11159. [CrossRef]
14. Gao, W.; An, Q.S.; Hao, M.H.; Sun, R.; Yuan, J.; Zhang, F.J.; Ma, W.; Min, J.; Yang, C.L. Thick-film organic solar cells achieving over 11% efficiency and nearly 70% fill factor at thickness over 400 nm. *Adv. Funct. Mater.* **2020**, *30*, 1908336. [CrossRef]
15. Camaioni, N.; Carbonera, C.; Ciammaruchi, L.; Corso, G.; Mwaura, J.; Po, R.; Tinti, F. Polymer solar cells with active layer thickness compatible with scalable fabrication processes: A meta-analysis. *Adv. Mater.* **2023**, *35*, 2210146. [CrossRef]
16. Pan, F.L.; Luo, M.; Liu, X.C.; Jiang, H.Y.; Wang, Z.; Yuan, D.; Wang, Q.; Qing, L.C.; Zhang, Z.S.; Zhang, L.J.; et al. Binary non-fullerene-based polymer solar cells with a 430 nm thick active layer showing 15.39% efficiency and 73.38% fill factor. *J. Mater. Chem. A* **2021**, *9*, 7129–7136. [CrossRef]
17. Yang, C.; Zhao, C.; Sun, Y.; Li, Q.; Islam, M.R.; Liu, K.; Wang, Z.; Qu, S.; Wang, Z. Optical management in organic photovoltaic devices. *Carbon Energy* **2021**, *3*, 4–23. [CrossRef]
18. Hu, T.; Zhang, M.; Mei, H.; Chang, P.; Wang, X.; Cheng, L. 3D printing technology toward state-of-the-art photoelectric devices. *Adv. Mater. Technol.* **2023**, *8*, 2200827. [CrossRef]
19. Jiang, S.; Wang, R.; Li, M.; Yu, R.; Wang, F.; Tan, Z.A. Synergistic electrical and light management enables efficient monolithic inorganic perovskite/organic tandem solar cells with over 24% efficiency. *Energy Environ. Sci.* **2024**, *17*, 219–226. [CrossRef]
20. Shi, Y.; Pan, J.; Yu, J.; Zhang, J.; Gao, F.; Lu, K.; Wei, Z. Optimizing the charge carrier and light management of nonfullerene acceptors for efficient organic solar cells with small nonradiative energy losses. *Sol. RRL* **2021**, *5*, 2100008. [CrossRef]
21. Hadipour, A.; de Boer, B.; Blom, P. Solution-processed organic tandem solar cells with embedded optical spacers. *J. Appl. Phys.* **2007**, *102*, 074506–074511. [CrossRef]
22. Roy, A.; Park, S.; Cowan, S.; Tong, M.; Cho, S.; Lee, K.; Heeger, A. Titanium suboxide as an optical spacer in polymer solar cells. *Appl. Phys. Lett.* **2009**, *95*, 013302. [CrossRef]
23. Ko, D.; Tumbleston, J.; Zhang, L.; Williams, S.; DeSimone, J.; Lopez, R.; Samulski, E. Photonic crystal geometry for organic solar cells. *Nano Lett.* **2009**, *9*, 2742–2746. [CrossRef] [PubMed]
24. Na, S.; Kim, S.; Jo, J.; Oh, S.; Kim, J.; Kim, D. Efficient polymer solar cells with surface relief gratings fabricated by simple soft lithography. *Adv. Funct. Mater.* **2008**, *18*, 3956–3963. [CrossRef]
25. Nalwa, K.; Park, J.; Ho, K.; Chaudhary, S. On realizing higher efficiency polymer solar cells using a textured substrate platform. *Adv. Mater.* **2011**, *23*, 112–116. [CrossRef] [PubMed]
26. Zhu, X.; Choy, W.; Xie, F.; Duan, C.; Wang, C.; He, W.; Huang, F.; Cao, Y. A study of optical properties enhancement in low-bandgap polymer solar cells with embedded PEDOT:PSS gratings. *Sol. Energy Mater. Sol. Cells* **2012**, *99*, 327–332. [CrossRef]
27. Wu, J.; Chen, F.; Hsiao, Y.S.; Chien, F.C.; Chen, P.; Kuo, C.; Huang, M.; Hsu, C.S. Surface plasmonic effects of metallic nanoparticles on the performance of polymer bulk heterojunction solar cells. *ACS Nano* **2011**, *5*, 959–967. [CrossRef]
28. Pastorelli, F.; Romero-Gomez, P.; Betancur, R.; Martinez-Otero, A.; Mantilla-Perez, P.; Bonod, N.; Martorell, J. Enhanced light harvesting in semitransparent organic solar cells using an optical metal cavity configuration. *Adv. Energy Mater.* **2015**, *5*, 1400614. [CrossRef]
29. Yang, Y.; Mielczarek, K.; Aryal, M.; Zakhidov, A.; Hu, W. Nanoimprinted polymer solar cell. *ACS Nano* **2012**, *6*, 2877–2892. [CrossRef] [PubMed]
30. Xie, L.; Song, W.; Ge, J.; Tang, B.; Zhang, X.; Wu, T.; Ge, Z. Recent progress of organic photovoltaics for indoor energy harvesting. *Nano Energy* **2021**, *82*, 105770. [CrossRef]

31. Li, C.; Tao, J.Y.; Zou, Z.J.; Liao, G.H.; Li, F.; Wang, J.F.; Sun, X.X.; Ni, J.; Zhang, J.J. Broad spectrum light-trapping ternary polymer solar cells based on self-assembled nano-ridged active layer. *Sol. Energy* **2020**, *198*, 1–7. [CrossRef]
32. Li, C.; Chen, M.; Li, F.; Sun, X.; Yu, Z.; Tao, J.; Zou, Z.; Liao, G.; Zhang, J. Simulation of light-trapping characteristics of self-assembled nano-ridges in ternary organic film. *Coatings* **2022**, *12*, 1340. [CrossRef]
33. Oskooi, A.F.; Roundy, D.; Ibanescu, M.; Bermel, P.; Joannopoulos, J.D.; Johnson, S.G. MEEP: A flexible free-software package for electromagnetic simulations by the FDTD method. *Comput. Phys. Commun.* **2010**, *181*, 687–702. [CrossRef]
34. Vedraine, S.; Torchio, P.; Duché, D.; Flory, F.; Simon, J.J.; Le Rouzo, J.; Escoubas, L. Intrinsic absorption of plasmonic structures for organic solar cells. *Sol. Energy Mater. Sol. Cells* **2011**, *95*, S57–S64. [CrossRef]
35. Duche, D.; Torchio, P.; Escoubas, L.; Monestier, F.; Simon, J.J.; Flory, F.; Mathian, G. Improving light absorption in organic solar cells by plasmonic contribution. *Sol. Energy Mater. Sol. Cells* **2009**, *93*, 1377–1382. [CrossRef]
36. Aguilar, O.; de Castro, S.; Godoy, M.P.F.; Dias, M.R.S. Optoelectronic characterization of $Zn_{1-x}Cd_xO$ thin films as an alternative to photonic crystals in organic solar cells. *Opt. Mater. Express* **2019**, *9*, 3638–3648. [CrossRef]
37. Shin, S.C.; Vincent, P.; Bae, J.H.; Lee, J.J.; Nam, M.; Ko, D.H.; Kim, H.; Shim, J.W. Quaternary indoor organic photovoltaic device demonstrating panchromatic absorption and power conversion efficiency of 10%. *Dyes Pigments* **2019**, *163*, 48–54. [CrossRef]
38. Razzell-Hollis, J.; Wade, J.; Tsoi, W.C.; Soon, Y.; Durrant, J.; Kim, J.S. Photochemical stability of high efficiency PTB7:PC_{70}BM solar cell blends. *J. Mater. Chem. A* **2014**, *2*, 20189–20195. [CrossRef]
39. Sharma, N.; Gupta, S.K.; Negi, C.M.S. New insights into the impact of graphene oxide incorporation on molecular ordering and photophysical properties of PTB7:C70 blends. *J. Mater. Sci. Mater. Electron.* **2020**, *31*, 22274–22283. [CrossRef]
40. Chen, J.D.; Cui, C.H.; Li, Y.Q.; Zhou, L.; Ou, Q.D.; Li, C.; Li, Y.F.; Tang, J.X. Single-junction polymer solar cells exceeding 10% power conversion efficiency. *Adv. Mater.* **2015**, *27*, 1035–1041. [CrossRef]
41. Palanchoke, U.; Jovanov, V.; Kurz, H.; Dewan, R.; Magnus, P.; Stiebig, H.; Knipp, D. Influence of back contact roughness on light trapping and plasmonic losses of randomly textured amorphous silicon thin film solar cells. *Appl. Phys. Lett.* **2013**, *102*, 083501. [CrossRef]
42. Qiu, W.; Xiao, S.; Tong, Y.; Yang, S. Toward efficient charge collection and light absorption: A perspective of light trapping for advanced photoelectrodes. *J. Phys. Chem. C* **2019**, *123*, 18753–18770. [CrossRef]